Formation of Local Resonance Band Gaps in Finite Acoustic Metamaterials: A Closed-form Transfer Function Model

H. Al Ba'ba'a[a], M. Nouh[a,*], T. Singh[a]

[a] *Dept. of Mechanical & Aerospace Engineering, Univeristy at Buffalo (SUNY), Buffalo, NY*

Abstract

The focus of this paper is on the use of transfer functions to comprehend the formation of band gaps in locally resonant acoustic metamaterials. Identifying a recursive approach for any number of serially arranged locally resonant mass in mass cells, a closed form expression for the transfer function is derived. Analysis of the end-to-end transfer function helps identify the fundamental mechanism for the band gap formation in a finite metamaterial. This mechanism includes (a) repeated complex conjugate zeros located at the natural frequency of the individual local resonators, (b) the presence of two poles which flank the band gap, and (c) the absence of poles in the band-gap. Analysis of the finite cell dynamics are compared to the Bloch-wave analysis of infinitely long metamaterials to confirm the theoretical limits of the band gap estimated by the transfer function modeling. The analysis also explains how the band gap evolves as the number of cells in the metamaterial chain increases and highlights how the response varies depending on the chosen sensing location along the length of the metamaterial. The proposed transfer function approach to compute and evaluate band gaps in locally resonant structures provides a framework for the exploitation of control techniques to modify and tune band gaps in finite metamaterial realizations.

Keywords: acoustic metamaterials, band gaps, transfer functions

1. Introduction

Acoustic metamaterials (AMMs) are sub-wavelength structures that consist of a chain of self-repeating unit cells which house internal elastic resonators. The hallmark feature of AMMs is their ability to realize band gaps, i.e. regions of blocked wave propagation, in low frequency regimes. Band gaps in AMMs primarily depend on the resonator properties and are, thus, size-independent and mechanically tunable [1]. Unique wave propagation behavior in AMMs

*Corresponding author
Email address: mnouh@buffalo.edu (M. Nouh)

have rendered them appealing for a wide range of damping and noise control applications. Over the past few decades, AMMs have been investigated in the context of discrete lumped mass systems [2, 3], elastic bars [4, 5], flexural beams [6–14], as well as 2D membranes and plates [15–18]. Given the dependence of the band structure of the AMM unit cell on resonator parameters, multiple efforts have also been placed on piezoelectric, or actively controlled, metamaterials [19–23].

Acoustic metamaterials are most commonly modeled using a Bloch-wave propagation model of the self-repeating unit cell with infinitely periodic boundary conditions [24, 25], or similarly using a Transfer Matrix Method [26–28]. Wave propagation methods assume traveling wave propagation in an infinitely-long metamaterial comprised of the individual unit cells. Local resonance band gaps in these infinite structures has been explained in light of gaps in the unit cell's dispersion curve (band diagram) and/or the negative effective mass density concept [29, 30]. To this date, however, a mathematical framework that explains and quantifies the formation of these band gaps in physical realizable finite locally resonant structures is lacking. In this effort, we focus on finite AMMs where the number of cells, as well excitation and response locations, are specified. We derive a generalized dynamic model to evaluate the input-to-output transfer function associated with such locally resonant structures, and explain the formation mechanism of the band gap in light of their frequency response and pole-zero (PZ) distributions. To facilitate the discussion, the analysis herein is presented on a one-dimensional mass-in-mass type metamaterial. The AMM consists of a chain of spring-mass unit cells shown in Figure 1. In the presented analysis, damping elements are excluded from both the base and the local structure for two important reasons: (1) to neutralize the effect of dissipation on the band gaps, an effect that has been recently investigated in a number of efforts [31–34], and (2) to ensure that any damping captured in the numerically computed poles or zeros in the lengthy expressions of the developed dynamic model of the finite AMM are merely a result of minor errors due to limited computational precision, as will be highlighted later in the discussion. The discussion is also extended to explain and differentiate between the effects of sensing location (i.e., location where displacement is measured) and the effect of the number of cells on the bandwidth and degree of attenuation obtained from the local resonators. Analysis of AMMs from a dynamic systems perspective provides a physical insight into the formation of these band gaps over a specific range of frequencies, and provides a clear distinction between the operation concepts of AMMs and tuned dynamic absorbers from a vibrations standpoint. Furthermore, explaining the behavior in terms of frequency domain tools and PZ-maps sets a future framework for implementing control techniques. Finally, the investigation of finite metamaterial structures is naturally of interest since the results directly impact the fabrication of realistic and physically realizable, rather than purely theoretical, AMMs.

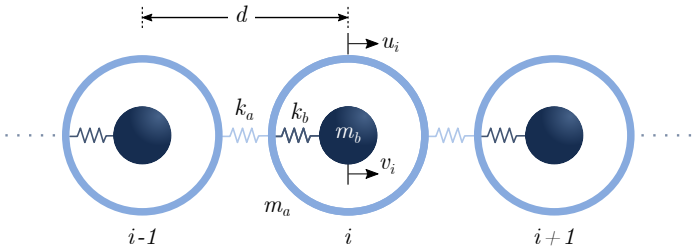

Figure 1: A lumped mass-in-mass locally resonant acoustic metamaterial

2. Dynamics of 1-D Acoustic Metamaterials

2.1. Wave Dispersion Analysis

The simplest example of an AMM is a periodic series of spring-mass systems hosting internal spring-mass resonators, as shown in Figure 1. For an AMM with cell spacing d, identical outer masses m_a and inner masses m_b connected via springs k_a and k_b, the governing motion equations for the i^{th} unit can be derived as:

$$\begin{bmatrix} m_a & 0 \\ 0 & m_b \end{bmatrix} \begin{Bmatrix} \ddot{u}_i \\ \ddot{v}_i \end{Bmatrix} + \begin{bmatrix} 2k_a + k_b & -k_b \\ -k_b & k_b \end{bmatrix} \begin{Bmatrix} u_i \\ v_i \end{Bmatrix} + \begin{bmatrix} -k_a & -k_a \\ 0 & 0 \end{bmatrix} \begin{Bmatrix} u_{i-1} \\ u_{i+1} \end{Bmatrix} = \begin{Bmatrix} 0 \\ 0 \end{Bmatrix} \quad (1)$$

where u_i and v_i represent the displacements of m_a and m_b of the i^{th} cell, respectively. By applying the harmonic wave solution to the above motion equations, the dispersion relation can be derived as [3]

$$A_1\omega^4 + A_2\omega^2 + A_3 = 0 \quad (2)$$

with

$$A_1 = m_a m_b, \quad A_2 = -[(m_a + m_b)k_b + 2m_b k_a(1 - \cos\bar{\beta})], \quad A_3 = 2k_a k_b(1 - \cos\bar{\beta})$$

where ω is the angular frequency and $\bar{\beta}$ is the normalized wavenumber given by $2\pi d/\lambda$ where λ is the wavelength, or the spatial period of the propagating wave. Equation (2) can be normalized in terms of the mass ratio $m_r = m_b/m_a$, the stiffness ratio $k_r = k_b/k_a$, and a non-dimensional frequency $\Omega = \omega/\omega_b$

$$\Omega^4 - [(1 + m_r) + 2\Gamma(1 - cos\bar{\beta})]\Omega^2 + 2\Gamma(1 - cos\bar{\beta}) = 0 \quad (3)$$

where $\omega_b = \sqrt{k_b/m_b}$ is the natural frequency of the local resonator and $\Gamma = \frac{m_r}{k_r}$. Eq. (3) can be used to compute the dispersion curves (band structure) $\Omega(\bar{\beta})$ of the AMM. Figure 2(a) shows these curves for an AMM with $m_a = 1$ kg, $m_b = 0.3m_a$, $k_a = 4.8$ GN/m and $k_b = 0.1k_a$. The shaded region represents the frequency range of the local resonance band gap which also spans the negative

effective mass m_e region of an equivalent homogeneous material, as shown in Figure 2(b), and given by [29]

$$m_e = m_a + \frac{m_b \omega_b^2}{\omega_b^2 - \omega^2}. \tag{4}$$

The band gap splits the dispersion curve of the metamaterial into acoustic and optic branches (where $\bar{\beta}$ is purely real) representing in-phase and out-of-phase propagating wave modes in the outer mass and the internal resonator. The theoretical bounds of the band gap can be obtained directly from Eq. (3). By setting $\bar{\beta} = \pi$, the solution of the dispersion relation yields the lower bound Ω_l which is, for this case, equal to 0.987. Generally, Ω_l will vary with both the stiffness and the mass ratios of the individual cell and is given by

$$\Omega_l = \frac{1}{\sqrt{2}} \sqrt{(1 + m_r + 4\Gamma) - \sqrt{(1 + m_r + 4\Gamma)^2 - 16\Gamma}} \tag{5}$$

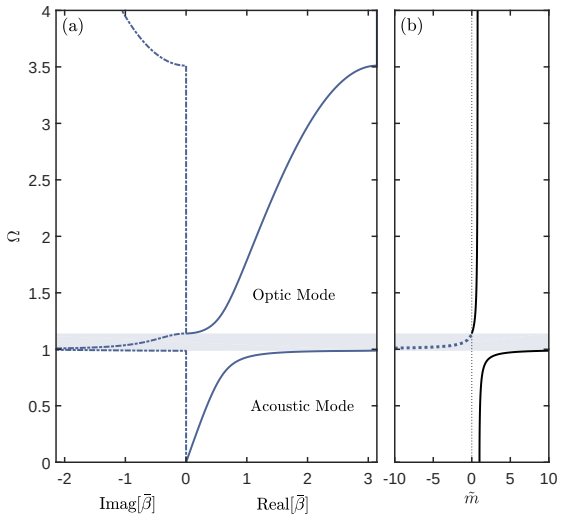

Figure 2: (a) Band structure of the AMM unit cell obtained from its dispersion relations and (b) the corresponding normalized effective mass $\tilde{m} = \frac{m_e}{(m_a + m_b)}$. The shaded region highlights the band gap frequency span in (a) showing that it matches the negative effective mass region in (b)

On the other hand, the upper bound of the band gap Ω_u can be obtained by setting $\bar{\beta} = 0$ to obtain a non-zero solution of

$$\Omega_u = \sqrt{1 + m_r} \tag{6}$$

which solely depends on the mass ratio m_r.

Figure (3) graphically depicts the effect of both the mass and stiffness ratios on the local resonance band gap bounds, which will be relevant to the discussion in Sec. 4. Important to note here is that the AMM band gap does not necessarily

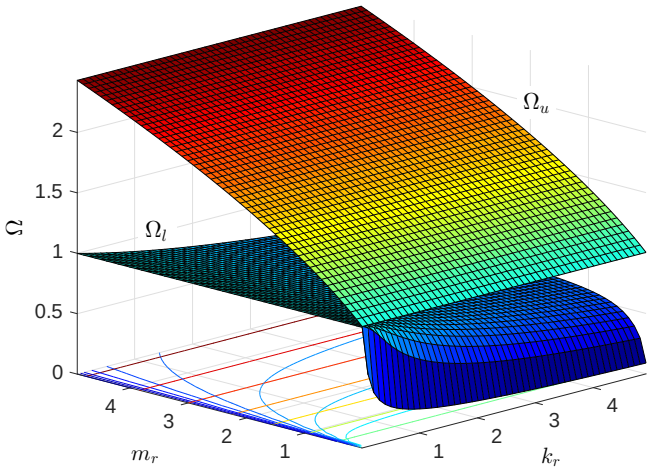

Figure 3: Change of the local resonance band gap bounds, Ω_l and Ω_u, with variation of m_r and k_r

start at the natural frequency of the local resonator (i.e. at $\Omega_l = 1$), which is a common misconception. It can be seen, however, that as k_r approaches zero, the solution of Ω_l in Eq. (5) approaches 1. However, a larger k_r shifts the lower end of the band gap down, effectively shortening the acoustic mode. In which case, the AMM band gap (and attenuation of incident waves) can start at a frequency lower than the local resonance. Although existent, the effect of m_r on Ω_l is however minimal. On the other hand, the upper bound of the band gap Ω_u is solely influenced by m_r which also shapes the final structure of the optic branch. Finally, it is worth noting that an exact $\Omega_l = 1$ value is not achievable from Eq. (5) for any combination of m_r and k_r. However, $\Omega_l = 0$ may be obtained as a result of a zero Γ and a non-zero m_r, (i.e. an infinitely stiff local spring), which is a purely theoretical case.

2.2. Structural dynamics of a finite AMM

Since the AMM in Figure 1 is described by a series of discrete mechanical elements, the profile of the propagating waves is captured by the discretized displacement field given by the vectors $\mathbf{u}$ and $\mathbf{v}$ along the length L of the AMM, where

$$\mathbf{u} = \begin{Bmatrix} u_1 & u_2 & \dots & u_i & \dots & u_n \end{Bmatrix}^T \tag{7}$$

and

$$\mathbf{v} = \begin{Bmatrix} v_1 & v_2 & \dots & v_i & \dots & v_n \end{Bmatrix}^T \tag{8}$$

For an AMM of n cells, the equations of motion of the end cells slightly differ

from middle ones. For any i^{th} cell where $2 \leq i \leq n-1$, the motion is given by

$$\begin{gathered} m_a\ddot{u}_i + (2k_a + k_b)u_i - k_a u_{i-1} - k_a u_{i+1} - k_b v_i = 0 \\ m_b\ddot{v}_i + k_b v_i - k_b u_i = 0 \end{gathered} \tag{9}$$

while the first ($i = 1$) and last ($i = n$) cells are described by

$$\begin{gathered} m_a\ddot{u}_1 + (k_a + k_b)u_1 - k_a u_2 - k_b v_1 = 0 \\ m_b\ddot{v}_1 + k_b v_1 - k_b u_1 = 0 \end{gathered} \tag{10}$$

and

$$\begin{gathered} m_a\ddot{u}_n + (k_a + k_b)u_n - k_a u_{n-1} - k_b v_n = 0 \\ m_b\ddot{v}_n + k_b v_n - k_b u_n = 0 \end{gathered} \tag{11}$$

As a result, the steady-state oscillations of a finite AMM subject to an external sinusoidal excitation $\mathbf{F}$ (applied to any outer mass) is given by

$$\begin{Bmatrix} \mathbf{u} \\ \mathbf{v} \end{Bmatrix} = \left(-\omega^2 \begin{bmatrix} \mathbf{M_u} & \mathbf{0} \\ \mathbf{0} & \mathbf{M_v} \end{bmatrix} + \begin{bmatrix} \mathbf{K_u} & -\mathbf{K_v} \\ -\mathbf{K_v} & \mathbf{K_v} \end{bmatrix} \right)^{-1} \begin{Bmatrix} \mathbf{F} \\ \mathbf{0} \end{Bmatrix} \tag{12}$$

where the sub-components of the mass and stiffness matrices can be obtained from

$$\underset{n\times n}{\mathbf{M_u}} = \begin{bmatrix} m_a & & & \\ & m_a & & \\ & & \ddots & \\ & & & m_a \end{bmatrix} \quad \underset{n\times n}{\mathbf{M_v}} = \begin{bmatrix} m_b & & & \\ & m_b & & \\ & & \ddots & \\ & & & m_b \end{bmatrix} \tag{13}$$

$$\underset{n\times n}{\mathbf{K_v}} = \begin{bmatrix} k_b & & & \\ & k_b & & \\ & & \ddots & \\ & & & k_b \end{bmatrix} \tag{14}$$

and

$$\underset{n\times n}{\mathbf{K_u}} = \begin{bmatrix} k_a + k_b & -k_a & & & \\ -k_a & 2k_a + k_b & -k_a & & \\ & \ddots & \ddots & \ddots & \\ & & -k_a & 2k_a + k_b & -k_a \\ & & & -k_a & k_a + k_b \end{bmatrix} \tag{15}$$

3. Transfer Functions and Pole/Zero Distribution

3.1. Transfer function of a 2-cell AMM

Starting with a 2-cell AMM of the same unit cell configuration (Figure 4(a)), we derive the transfer function relating the displacement of the second outer mass u_2 to an input force F applied to the first. The 2-cell constitutes a 4 degree-of-freedom (DOF) system, with the DOFs being the outer and inner displacements of the 2 cells. Following Eqs. (10) and (11), we can rewrite the motion equations in the Laplace domain via

$$U_1 = G(s)(k_a U_2 + k_b V_1 + F) \tag{16}$$

$$U_2 = G(s)(k_a U_1 + k_b V_2) \tag{17}$$

$$\frac{V_2}{U_2} = \frac{V_1}{U_1} = H(s) \tag{18}$$

where the upper case $U_i(s)$ and $V_i(s)$ represent the displacements $u_i(t)$ and $v_i(t)$ in the Laplace domain, written as U_i and V_i for brevity. And the transfer functions $G(s)$ and $H(s)$ are given by $\frac{1}{m_a s^2+(k_a+k_b)}$ and $\frac{k_b}{m_b s^2+k_b}$, respectively. The dynamics of the 2-cell AMM can be graphically represented using the block diagram shown in Figure 4(b). The end-to-end transfer function U_2/F can be obtained from Eqs. (16) through (18) or by reducing the shown block diagram as will be presented next. We will use the block diagram reduction approach as it reveals some trends and consistent patterns in the dynamics of this class of locally resonant metamaterials that will be later used to generalize this framework for an AMM with any n number of cells.

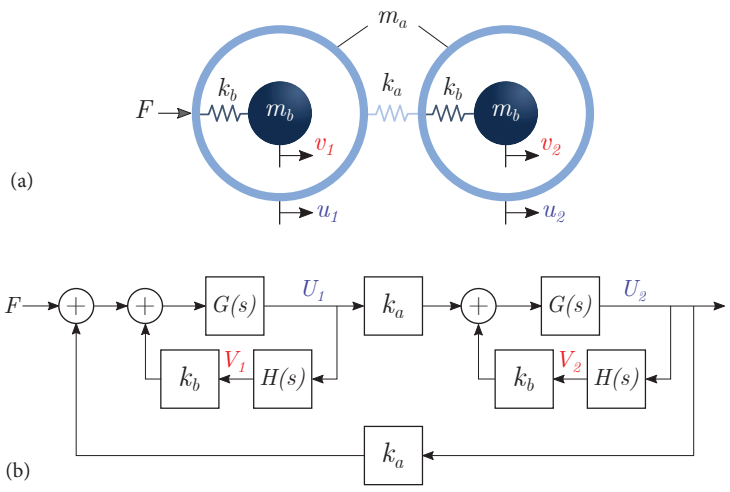

Figure 4: (a) Schematic and (b) Block diagram of a 2-cell locally resonant AMM

Moving the feedback gain k_a to the forward path, and make the necessary adjustments, reduces the system to the diagram in Figure 5. The dotted boxes represent similar structures and can be replaced with the single transfer function T_1 as shown in Figure 6.

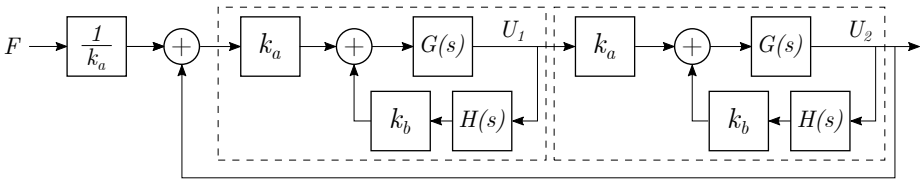

Figure 5: Block diagram of the 2-cell AMM reduced from Figure 4(b)

T_1 simplifies Eqs. (16) and (17) to the following form

$$U_1 = T_1(s)(U_2 + F(s)/k_a) \tag{19}$$

$$U_2 = T_1(s)U_1 \tag{20}$$

and is given by

$$T_1 = \frac{\alpha_1 s^2 + \alpha_2}{s^4 + \alpha_3 s^2 + \alpha_2} \tag{21}$$

where $\alpha_1 = \omega_a^2 = \frac{k_a}{m_a}$, $\alpha_2 = \omega_a^2\omega_b^2$, and $\alpha_3 = \omega_a^2 + \omega_b^2 + k_b/m_a$. Reducing Figure 6 to a single block gives the transfer function U_2/F

$$\frac{U_2}{F} = \frac{(\alpha_1 s^2 + \alpha_2)^2}{s^2(s^2 + (\alpha_3 - \alpha_1))(s^4 + (\alpha_3 + \alpha_1)s^2 + 2\alpha_2)} \tag{22}$$

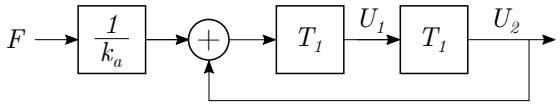

Figure 6: Block diagram of the 2-cell AMM reduced from Figure 5

The dynamics of the 2-cell AMM captured by Eq. (22) is graphically represented in Figure 7, for the same values of m_a, m_b, k_a, and k_b used earlier to plot the dispersion curves. As depicted in the transfer function, the AMM has two repeated poles at $s = 0$ and at $s = \pm j\omega_b\sqrt{1 + m_r}$ (p_1 and p_3 in Figure 7). The poles at the origin are representative of the AMM's rigid body modes since the system considered is unconstrained (i.e. free-free). The poles at $\pm j\omega_b\sqrt{1 + m_r}$ indicate the presence of a resonant frequency of the 4-DOF AMM right at the upper bound of the band gap, as given earlier by Eq. (6). The significance of the remaining poles will become clear later when the general case of an AMM with a n number of cells is discussed. On the other hand, the 2-cell AMM has

repeated zeros at $s = \pm j\omega_b$ which is the stand-alone natural frequency of the local resonator. In this case, the 2-cell AMM acts as a tuned absorber with

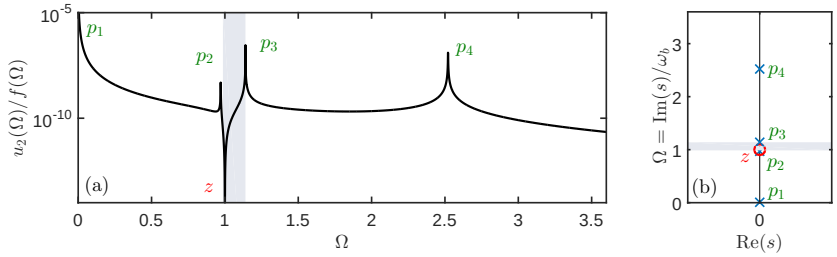

Figure 7: (a) Frequency response of the outer displacement of the second cell u_2 in a 2-cell AMM as a ratio of the input force f. (b) Corresponding pole-zero map of the U_2/F transfer function shown in Eq. (22). p and z denote the locations of the poles and zeros, respectively. The shaded region in both plots represents the band gap span of an infinite AMM as predicted by the unit cell dispersion relations in Figure 2

3.2. General formulation for an n-cell AMM

Using a similar approach, and by utilizing the repeating patterns in the block structure of the AMM, a closed-form expression for the transfer function of a general lumped AMM with any given n number of cells can be derived. The obtained transfer function can specifically describe the displacement of any i^{th} cell in the AMM to a given forcing input. In the next steps, the exciting force F is still applied to the outer mass of the first AMM cell. Owing to the periodic nature of the AMM, the block diagram of n cells is now presented by a series of nested unity feedback loops with two forward path transfer functions T_1 and T_2, as shown in Figure 8. T_2 is given by

$$T_2 = \frac{\alpha_1 s^2 + \alpha_2}{s^4 + (\alpha_1 + \alpha_3)s^2 + 2\alpha_2} \tag{23}$$

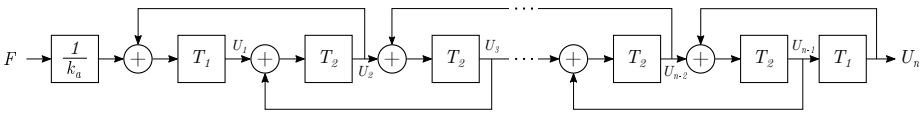

Figure 8: Block diagram of an n-cell AMM

One way to obtain an expression for the end-to-end transfer function U_n/F is to move the feedback branch from U_n to the left of last T_1 block. A reduced feedback loop B_{n-1}, highlighted in Figure 9, can be generated as a result. Note that the last block in Figure 9 is $B_n = T_1$. Moving backward and repeating this

procedure yields another reduced block B_{n-2} that is a function of B_{n-1}, and so on. This process can be repeated n times going back all the way to the force input. The final form is shown in Figure 10, where B_n is equal to T_1.

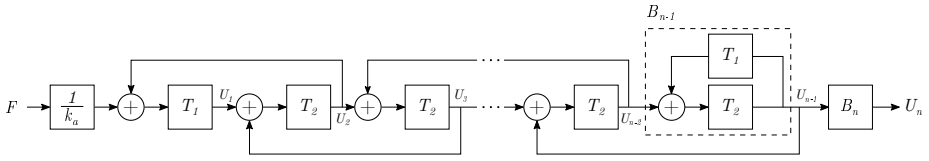

Figure 9: Block diagram of an n-cell AMM reduced from Figure 8

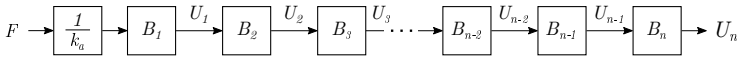

Figure 10: Block diagram of an n-cell AMM reduced from Figure 9

This repetitive process of computing the equivalent transfer function of the closed loop is found to be analogous to the continuous fraction technique [35], which can be used to obtain a general formula for the block $B_{n-(j+1)}$, as shown in Figure 11.

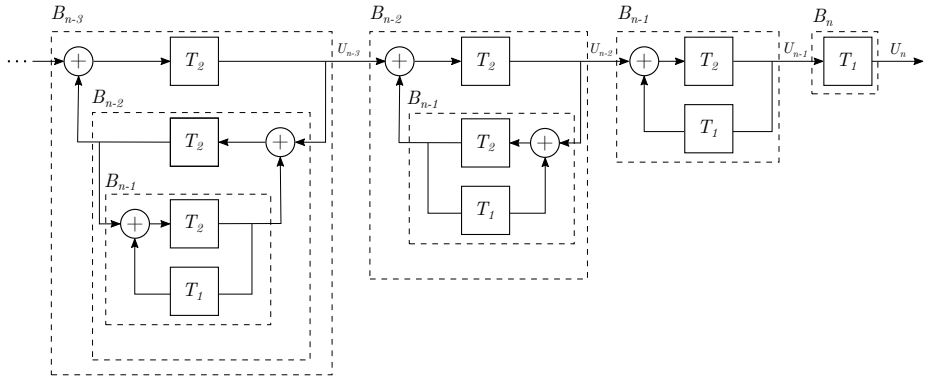

Figure 11: A continuous fraction model for an n-cell AMM

Figure 11 can be mathematically expressed as

$$\frac{U_{n-(j+1)}}{U_{n-(j+2)}} = B_{n-(j+1)} =$$

$$\cfrac{1}{\cfrac{1}{T_{2-\delta_{j,(n-2)}}} - \left\{\cfrac{1}{\cfrac{1}{T_2} - \left\{\cfrac{1}{\cfrac{1}{T_2} - \left\{\cfrac{1}{\ddots - \left\{\cfrac{1}{\cfrac{1}{T_2} - T_1}\right\} j=0}\right\} \vdots}\right\} j-2}\right\} j-1}\Bigg\} j \tag{24}$$

where $j = 0, 1, 2, ..., (n-2)$, and $\delta_{j,(n-2)}$ is the Kronecker delta function which is equal to 1 when $j = (n-2)$ and is 0 otherwise. For $j = (n-2)$, $U_{n-(j+2)}$ is equal to

$$U_0 = \frac{F}{k_a}. \tag{25}$$

For example, for an AMM with 3 cells, we have $n = 3$. This results in

$$B_n = B_3 = T_1 \tag{26}$$

$$j = 0 \neq (n-2) \quad B_{n-(j+1)} = B_2 = \frac{1}{\cfrac{1}{T_2} - T_1} = \frac{T_2}{1 - T_1 T_2} \tag{27}$$

$$j = 1 = (n-2) \quad B_{n-(j+1)} = B_1 = \frac{1}{\cfrac{1}{T_1} - \cfrac{1}{\cfrac{1}{T_2} - T_1}} = \frac{T_1(1 - T_1 T_2)}{1 - 2T_1 T_2} \tag{28}$$

which gives us the transfer functions:

$$\frac{U_3}{F} = \frac{1}{k_a} B_1 B_2 B_3 = \frac{1}{k_a} \frac{T_1^2 T_2}{1 - 2T_1 T_2} \tag{29}$$

$$\frac{U_2}{F} = \frac{1}{k_a} B_1 B_2 = \frac{1}{k_a} \frac{T_1 T_2}{1 - 2T_1 T_2} \tag{30}$$

$$\frac{U_1}{F} = \frac{1}{k_a} B_1 = \frac{1}{k_a} \frac{T_1(1 - T_1 T_2)}{1 - 2T_1 T_2}. \tag{31}$$

Consequently, and as can be inferred from Figure 10, the transfer function relating the displacement of the k^{th} cell to the force F applied at the first cell can be computed using the following sequence product

$$\frac{U_k}{F} = \frac{1}{k_a} \prod_{j=0}^{k-1} B_{j+1} \tag{32}$$

3.3. Frequency Response Functions

The different frequency response functions (FRFs) of the AMM can be obtained by substituting $s = j\omega$, where ω is the driving frequency, and writing T_1 and T_2 in the frequency domain. Dividing throughout by ω_b^4 and a few further manipulations, we obtain

$$T_1 = \frac{\Gamma(1-\Omega^2)}{\Omega^4 - (\Gamma + m_r + 1)\Omega^2 + \Gamma} \tag{33}$$

and

$$T_2 = \frac{\Gamma(1-\Omega^2)}{\Omega^4 - (2\Gamma + m_r + 1)\Omega^2 + 2\Gamma} \tag{34}$$

For any n number of cells, the equivalent FRF of U_n/F is given by the following expression

$$\frac{U_n}{F} = \frac{Z_n(\Omega)}{P(\Omega)} = \frac{\Gamma^n(1-\Omega^2)^n}{k_a\Omega^2(\Omega^2 - (m_r+1))(\Omega^{4n-4} + \gamma_1\Omega^{4n-6} + ... + \gamma_{2n-1}\Omega^2 + \gamma_{2n})} \tag{35}$$

The FRF U_i/F for any intermediate cell i can be be found, by replacing the multiplication limit $n-1$ with $i-1$ in Eq. (32), to be

$$\frac{U_i}{F} = \frac{Z_i(\Omega)}{P(\Omega)} = \frac{\Gamma^i(1-\Omega^2)^i(\Omega^{4(n-i)} + \mu_1\Omega^{4(n-i)-2} + ... + \mu_{2(n-i)-1}\Omega^2 + \mu_{2(n-i)})}{k_a\Omega^2(\Omega^2 - (m_r+1))(\Omega^{4n-4} + \gamma_1\Omega^{4n-6} + ... + \gamma_{2n-1}\Omega^2 + \gamma_{2n})} \tag{36}$$

In Eqs. (35) and (36), γ_q and μ_p are a non-zero parameters for all given values of q and p, where $q = 1, 2, 3, ...2n$ and $p = 1, 2, 3, ..., 2(n-i)$. Two observations can be made on how Eq. (36) compares to Eq. (35): (A) The term $(1-\Omega^2)$ in both numerators yields the repeated zeros at $\Omega = 1$. Since $i < n$, the number of these repeated zeros for the U_i/F transfer function are less than its U_n/F counterpart. (B) The repeated zeros at $\Omega = 1$ are the only numerator roots for U_n/F, while a number of anti-resonances are sandwiched in between the resonant frequencies as evident by the last term in the numerator of U_i/F. These differences exemplify the effect of changing the sensor location on the system's transfer function, i.e., the effect of changing the cell of which the displacement is calculated. Both observations will be depicted clearly in the numerical examples presented in the forthcoming section.

4. Numerical Validation

4.1. Increasing the number of cells

We start by considering the AMM shown in Figure 1 with four different number of cells: $n = 2$, 5, 20 and 50. The value of the four cell parameters m_a, m_b, k_a, and k_b are kept the same as those used earlier. Throughout this section, the focus is on the behavior of the last cell in the AMM chain in response to a force applied at the very first cell. For a sinusoidal force with a 1 N amplitude sweeping the frequency range $0 < \Omega < 3.5$, the frequency response of the displacements of the inner and outer masses of the last cell in each case is displayed in Figure 12. These FRFs can be directly obtained from the harmonic analysis described in Eq.(12) or, equivalently, from the transfer function derived in Eq.(35). At a first glance, the plots show that as the number of cells of the AMM increases, the width of the zeroed out part of the response gradually increases and eventually spans the theoretically predicted band gap range of an infinite AMM, represented by the shaded region in Figure 12. In other words, the AMM departs from its ability to perfectly absorb an incident excitation at a single tuned frequency (earlier shown to be the natural frequency of the local resonator) to a structure which is able to almost perfectly absorb any incident waves over a continuous frequency range, a behavior which best describes the commonly known metamaterial band gap.

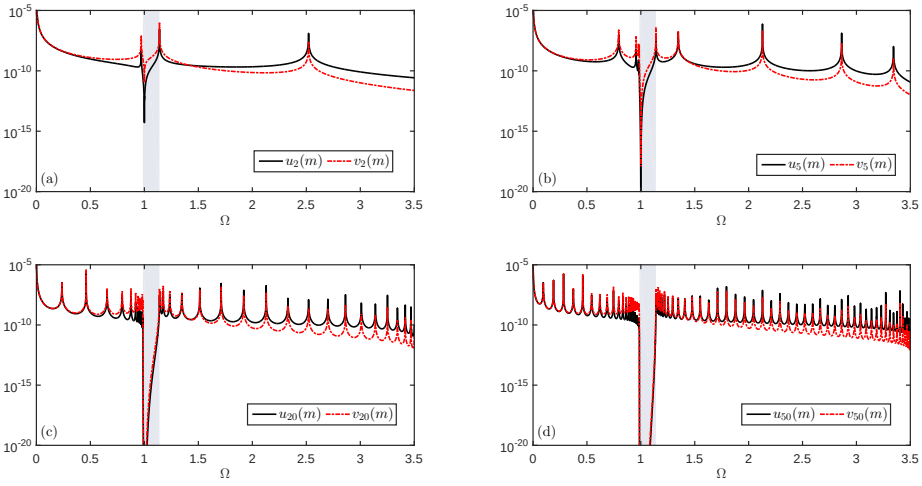

Figure 12: Frequency response of the outer and inner masses of the last cell, u_n and v_n, to an external force applied to the first cell for an AMM with (a) $n = 2$, (b) 5, (c) 20, and (d) 50 cells

4.2. The formation mechanism of the band gap

The mechanism by which this transition happens and the emergence of a bang gap behavior in a finite locally resonant structure can be understood in

light of the transfer functions described earlier. The corresponding pole-zero maps for the considered four AMMs are shown in Figure 13. The formation of the band gap is the result of three distinct phenomena that take place simultaneously in the dynamics of the AMM system. We will go over each of them separately.

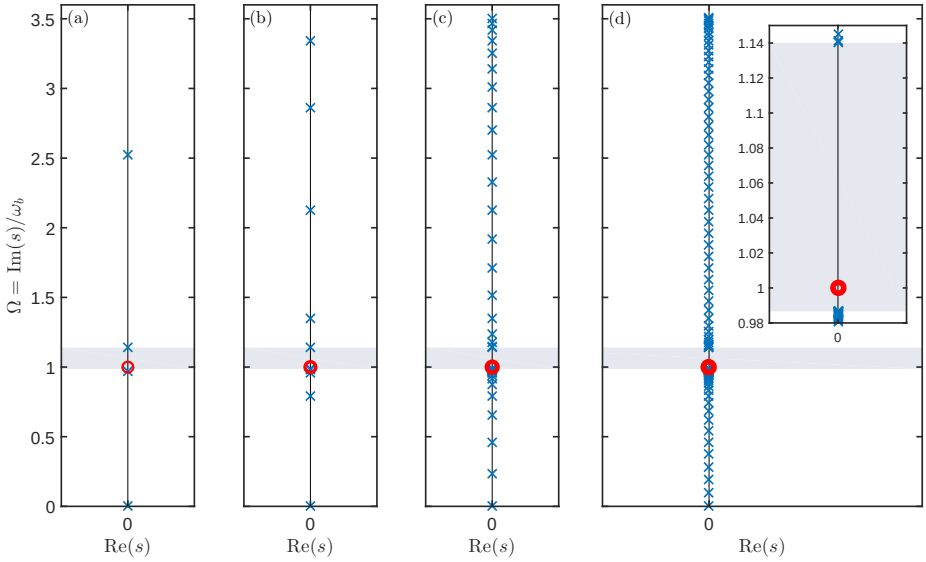

Figure 13: Pole-zero maps of the transfer function U_n/F for an AMM with (a) $n = 2$, (b) 5, (c) 20 and (d) 50 cells. Poles and zeros are marked with crosses and circles, respectively. A thicker zero marker indicates larger algebraic multiplicity at $\Omega = 1$.

4.2.1. The multiplicity effect of the locally resonant zero

As predicted by the derived transfer function in Eq. (35), increasing the number of cells of the AMM does not add zeros at new locations but rather increases the number of the repeated zeros at $\Omega = 1$. While obvious from the numerator of the derived function, the fact that a locally resonant AMM with any n number of cells has only one distinct zero location can be lost if the analysis is solely based on a numerical simulation. Figure 14 shows a common discrepancy obtained when using MATLAB's *pzmap* operator to obtain the distribution of zeros for this same example. The figure, incorrectly, shows several zeros both above and below $\Omega = 1$ with non-zero real components. Since the AMM under consideration is non-dissipative and lacks any damping elements, the roots of both the numerator and the denominator of the closed-form transfer function have to be purely imaginary (i.e. lie on the imaginary axis of the s-plane). The shown behavior is a result of numerical inaccuracies in the algorithm used by MATLAB to compute zeros in a system with high zero-multiplicity, which results in a cluster of approximate zeros distributed on a circle with a radius that is proportional to the machine precision [36]. This further signifies the im-

portance of independently deriving the closed-form expression for the AMM's transfer function using the presented block diagram approach to eventually draw accurate conclusions.

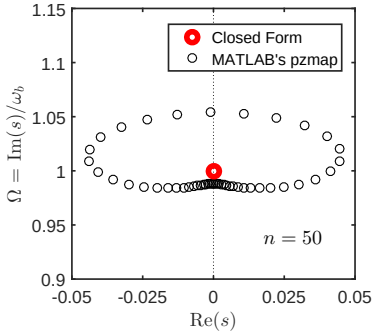

Figure 14: Zeros of the transfer function U_n/F of an AMM with $n = 50$ as calculated using the closed-form expression in Eq. (35) and numerically using MATLAB's *pzmap* operator

Since the AMM's transfer function has a distinct zero location at $\Omega = 1$, it technically has a single absolute zero frequency which is ω_b. Increasing the number of repeated zeros or numerator roots (commonly known as the algebraic multiplicity) only tends to flatten out the branches of the FRF around the zero location. The degree by which the branches bend outwards increases with the increase of the multiplicity or, in this case, the number of cells. As the number of cells approaches infinity, the numerator $Z_n(\Omega)$ in Eq. (35) approaches zero for any frequency Ω as long as the value of $\Gamma|(1-\Omega^2)|$ remains less than 1. Hence, this multiplicity effect is theoretically bounded by the range

$$\sqrt{1-\frac{1}{\Gamma}} < \Omega < \sqrt{1+\frac{1}{\Gamma}} \tag{37}$$

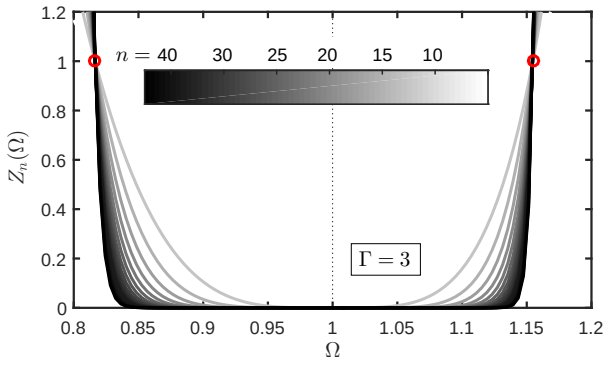

Figure 15: The effect of increasing the number of repeated roots (multiplicity) in numerator of the polynomial $Z_n(\Omega)$ with the increase in the number of cells n in an AMM with $\Gamma = 3$

Figure 15 shows the variation of $Z_n(\Omega)$ with the number of cells n for $\Gamma = 3$. It can be seen that even though the AMM has a single zero location at $\Omega = 1$, increasing n gradually increases the frequency range over which Z_n approaches zero via the multiplicity effect, thus widening the potential region over which the vibrations can be largely attenuated. This concept of placing multiple zeros has been exploited for robust time-delay filter design for shaping reference inputs to minimize residual vibrations of lightly damped structures [37, 38]. This effect however, as predicted, is limited to the region bounded by Eq. (37) which, in this case, corresponds to $0.816 < \Omega < 1.154$. Also worth noting, is the fact that all curves in Figure 15 with different multiplicity orders intersect at $\Omega = \sqrt{1 - \frac{1}{\Gamma}}$ and $\Omega = \sqrt{1 + \frac{1}{\Gamma}}$, for values of Γ greater than 1. However, the lower bound on the multiplicity effect cease to exist for $\Gamma < 1$, as shown in Figure 16.

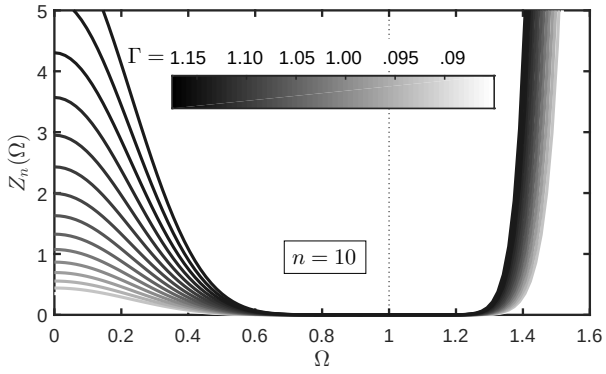

Figure 16: The effect of varying Γ on the numerator polynomial $Z_n(\Omega)$ for an AMM with a fixed number of cells ($n = 10$)

4.2.2. The enforced poles at the band gap bounds

The multiplicity range derived in Eq. (37) does not match the theoretical band gap bounds derived in Eqs. (5) and (6), and later observed in the FRFs of Figure 12(d) for a sufficiently large number of cells. In fact, Figs. 15 and 16 suggest that the band gap can extend well beyond the FRF limits if the analysis is solely based on the transfer function zeros. The second factor contributing to the formation of the band gap, as predicted theoretically, is the location of the transfer function poles in the vicinity of $\Omega = 1$. Eq. (35) shows that the roots of the characteristic polynomial $P(\Omega)$ of the transfer function U_n/F contains a set of repeated poles at $\Omega_u = \sqrt{1 + m_r}$. By knowing the value of the AMM masses, and hence m_r, the location of these poles can be determined and will be fixed irrespective of the number of cells n. The peak at $\Omega_u = \sqrt{1 + m_r}$ can be, therefore, clearly seen in all four subplots of Figure 12. The location of these poles precisely coincides with Ω_u, the upper band gap bound of the infinite AMM. This means that as the multiplicity of zeros attempts to flatten out the

frequency response curve around $\Omega = 1$, this effect is abruptly terminated at $\Omega_u = \sqrt{1 + m_r}$ due to the presence of a resonant frequency of the bulk structure. The FRF responds by moving quickly from a near-zero oscillation to a state of resonance and an extremely large amplitude. The same behavior takes place at the other end of the band gap thus constituting the formation of what appears to be a zeroed response over a continuous frequency range, or the band gap. The lower bound of the band gap, Ω_l, is also a pole that can be obtained from the last expression in the characteristic polynomial $P(\Omega)$ of order $4n - 4$. Unlike Ω_u, this pole is not fixed and moves slowly with changing n. Using a high-precision mathematical solver, the largest pole before the band gap can be computed. Although local resonance band gaps are commonly understood to start at $\Omega = 1$, Ω_l is actually always going to be smaller than 1. In this example, for $n = 50$, Ω_l is calculated to be 0.9866 to the nearest 4th decimal place. Figure 17 shows the convergence rate of Ω_l with respect to the number of cells n as well as the effect of changing the stiffness ratio k_r, as compared to the fixed Ω_u. For a sufficiently large number of cells, Ω_l approaches 1 and the band gap nearly realizes the theoretical bandwidth predicted by the dispersion analysis.

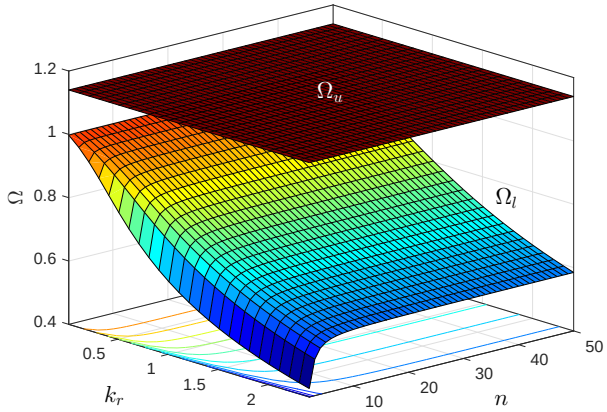

Figure 17: Convergence of Ω_l to 1 as n approaches infinity. Invariance of Ω_u with respect to n and k_r shown for comparison

4.2.3. The absence of poles in the band gap range

The last phenomenon that factors into the formation of the band gap in a finite AMM is the absence of resonances in the band gap frequency range. The pole-zero map in Figure 13 interestingly shows that, irrespective of the n of cells that constitute the AMM, the overall system poles are equally split around the band gap range with no poles lying in the shaded region. In the previous section, it was explained how the presence of two resonance peaks flanking the repeated zeros at $\Omega = 1$, define the bandwidth of the band gap. This last phenomenon is, therefore, essential to ensure that the multiplicity effect which contributes to extending the effect of the single zero location over the entire band gap range

is not interrupted within the band gap. Finally, by adopting a linear scale and a close-up of the FRFs, Figure 18 nicely illustrates the evolution of the band gap from a single anti-resonance (for an AMM with $n = 2$) to a continuous attenuation over an extended range ($n = 50$).

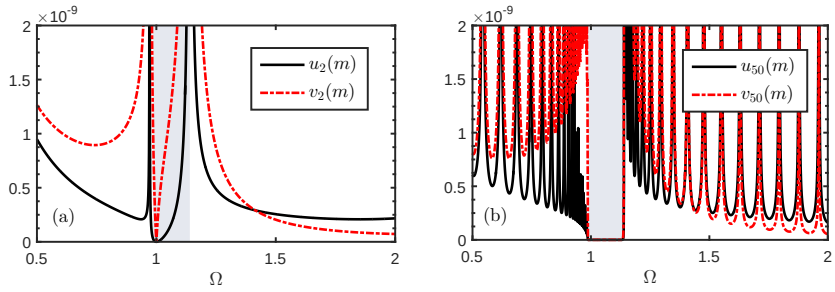

Figure 18: Evolution of the local resonance band gap in finite metamaterials from a (a) 2-cell AMM to a (b) 50-cell AMM.

4.3. Effect of sensor location

In this section, we examine the spatial attenuating of the propagating wave from the excitation location at one end of the AMM to different locations along the length of the AMM. Hence, we shift our focus to the transfer function U_i/F derived in Eq. (36). For an AMM with $n = 10$ cells and the same values for the cell parameters m_a, m_b, k_a, and k_b, Figure 19(a) through (d) shows the frequency responses of the 1^{st}, 4^{th}, 7^{th} and 10^{th} (and last) cells, respectively, to an external force acting on the outer mass of the 1^{st} cell. The corresponding pole-zero maps are displayed in Figure 20.

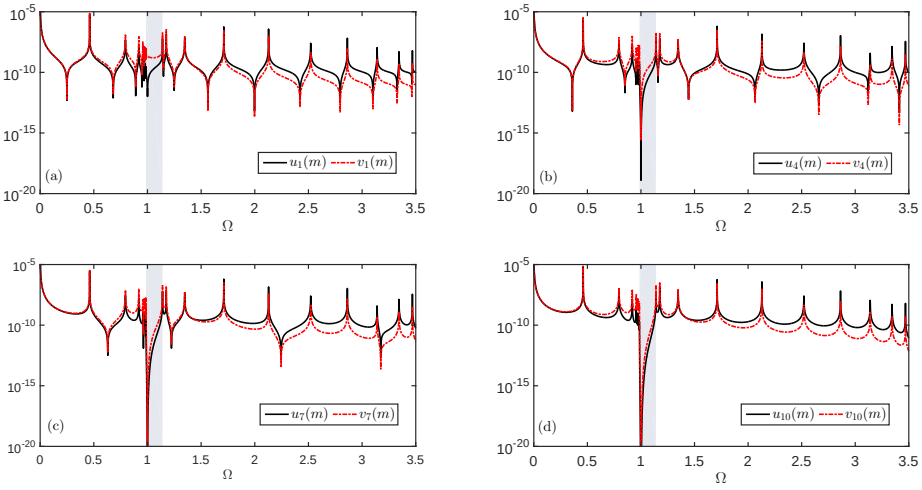

Figure 19: Frequency response of the outer and inner masses, u_i and v_i, of the (a) 1st, (b) 4th, (c) 7th, and (d) 10th (last) cell in an AMM with $n = 10$ cells

The FRFs shown in Figure 19 show that the degree of attenuation in the AMM increases as we move further away from the source, i.e., as i approaches n. From a transfer function perspective, the order of zero multiplicity (number of repeated zeros at $\Omega = 1$) is the same order as i, as captured by the $\Gamma^i(1-\Omega^2)^i$ term in the numerator $Z_i(\Omega)$ of Eq. (36). As the sensor is moved closer to the exciting force (i.e. as i approaches 1), some of these repeated zeros migrate to locations sandwiched between the system's poles. For a perfectly collocated sensor an actuator, each set of 2 neighboring poles will be separated by at least one zero. This zero migration behavior has been highlighted in literature in the context of controlled flexible structures [39, 40].

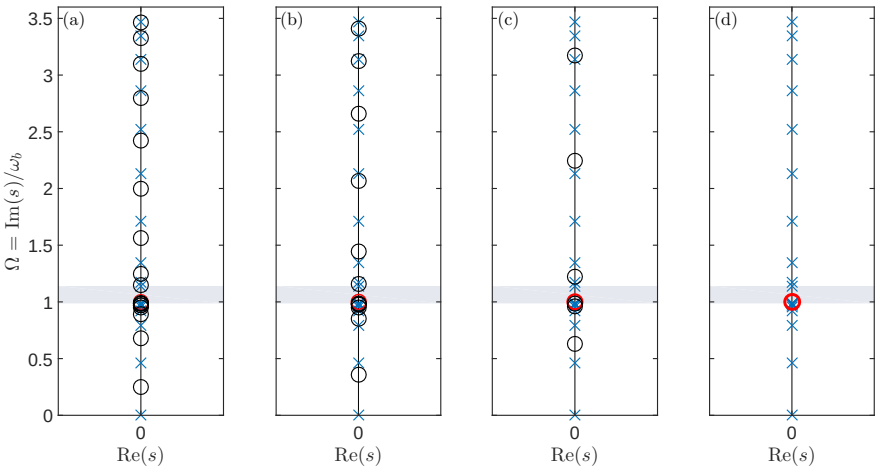

Figure 20: Pole-zero maps of the transfer function $\frac{U_i}{F}$ at i equal to (a) 1, (b) 4, (c) 7, and (d) 10 for a LREM with 10 cells. The red circles represents the zeros located at $\Omega = 1$, while the black ones are for the zeros caused from moving the measurement location.

5. Conclusions

This paper has presented an in-depth analysis of the formation of local resonance band gaps in locally resonant acoustic metamaterials of a finite length. A block diagram reduction approach was used to derive closed-form expressions for a lumped AMM with any n number of cells as well as at any cell location i. By deriving closed-form expressions for the force to end-displacement transfer functions, the frequency response of an AMM with a given set of parameters was obtained. The presented framework explained how the evolution of the band gap from a single anti-resonance to an attenuation of incident excitations over a continuous frequency range. The results are matched with the theoretical bounds of the band gap as derived by the commonly adopted Bloch-wave model and the dispersion relations for a traveling wave in an infinitely-long metamaterial. The emergence of the local resonance band gap was explained

using the derived system dynamics in light of three separate, yet simultaneous, phenomenon:

1. The existence of an n^{th} order multiplicity of repeated zeros at the distinct location of the local resonator ω_b which flattens out the FRF curves of the AMM's displacement, thus zeroing out the response around $\Omega = 1$.
2. The existence of system poles at both ends of the band gap that break the multiplicity effect. The pole north of the band gap is a fixed resonance at Ω_u that is independent of the number of cells and is solely a function of the mass ratio, while that south of the band gap varies with the AMM size and approaches 1 at sufficiently large values of n.
3. The distribution of poles on both sides of the band gap giving rise to different acoustic and optic resonant modes with the absence of any other poles in the band gap region.

The presented results facilitate the understanding of this type of local resonance band gaps in finite structures from a vibrations, rather than a wave-propagation standpoint. The study bridges the gap between the dispersion of waves in theoretical infinite structures and the structural dynamics of a finite, and thus physically realizable, metamaterial. Finally, investigating AMMs in the context of frequency domain tools and PZ-maps sets a future framework for implementing robust control techniques.

References

[1] Liu Z, Zhang X, Mao Y, Zhu Y, Yang Z, Chan CT, et al. Locally resonant sonic materials. Science 2000;289(5485):1734–6.

[2] Huang HH, Sun CT. A study of band-gap phenomena of two locally resonant acoustic metamaterials. Proceedings of the Institution of Mechanical Engineers, Part N: Journal of Nanoengineering and Nanosystems 2011;:1740349911409981.

[3] Huang GL, Sun CT. Band Gaps in a Multiresonator Acoustic Metamaterial. Journal of Vibration and Acoustics 2010;132(3):031003. doi:10.1115/1.4000784.

[4] Wang G, Yu D, Wen J, Liu Y, Wen X. One-dimensional phononic crystals with locally resonant structures. Physics Letters A 2004;327(5):512–21.

[5] Xiao Y, Wen J, Wen X. Longitudinal wave band gaps in metamaterial-based elastic rods containing multi-degree-of-freedom resonators. New Journal of Physics 2012;14(3):033042.

[6] Yu D, Liu Y, Zhao H, Wang G, Qiu J. Flexural vibration band gaps in euler-bernoulli beams with locally resonant structures with two degrees of freedom. Physical Review B 2006;73(6):064301.

[7] Yu D, Liu Y, Wang G, Zhao H, Qiu J. Flexural vibration band gaps in timoshenko beams with locally resonant structures. Journal of Applied Physics 2006;100(12):124901.

[8] Sun H, Du X, Pai PF. Theory of metamaterial beams for broadband vibration absorption. Journal of Intelligent Material Systems and Structures 2010;.

[9] Nouh M, Aldraihem O, Baz A. Vibration Characteristics of Metamaterial Beams With Periodic Local Resonances. Journal of Vibration and Acoustics 2014;136(6):61012. doi:10.1115/1.4028453.

[10] Pai PF, Peng H, Jiang S. Acoustic metamaterial beams based on multi-frequency vibration absorbers. International Journal of Mechanical Sciences 2014;79:195–205.

[11] Khajehtourian R, Hussein M. Dispersion characteristics of a nonlinear elastic metamaterial. AIP Advances 2014;4(12):124308.

[12] Xiao Y, Wen J, Yu D, Wen X. Flexural wave propagation in beams with periodically attached vibration absorbers: band-gap behavior and band formation mechanisms. Journal of Sound and Vibration 2013;332(4):867–93.

[13] Baravelli E, Ruzzene M. Internally resonating lattices for bandgap generation and low-frequency vibration control. Journal of Sound and Vibration 2013;332(25):6562–79. doi:10.1016/j.jsv.2013.08.014.

[14] Zhu R, Liu X, Hu G, Sun C, Huang G. A chiral elastic metamaterial beam for broadband vibration suppression. Journal of Sound and Vibration 2014;333(10):2759–73. doi:10.1016/j.jsv.2014.01.009.

[15] Krushynska A, Kouznetsova V, Geers M. Towards optimal design of locally resonant acoustic metamaterials. Journal of the Mechanics and Physics of Solids 2014;71:179–96.

[16] Peng H, Pai PF. Acoustic metamaterial plates for elastic wave absorption and structural vibration suppression. International Journal of Mechanical Sciences 2014;89:350–61.

[17] Wang Y, Wang Y. Complete bandgaps in two-dimensional phononic crystal slabs with resonators. Journal of Applied Physics 2013;114(4):043509.

[18] Nouh M, Aldraihem O, Baz A. Wave propagation in metamaterial plates with periodic local resonances. Journal of Sound and Vibration 2015;341:53–73. doi:10.1016/j.jsv.2014.12.030.

[19] Gonella S, To AC, Liu WK. Interplay between phononic bandgaps and piezoelectric microstructures for energy harvesting. Journal of the Mechanics and Physics of Solids 2009;57(3):621–33. doi:10.1016/j.jmps.2008.11.002.

[20] Celli P, Gonella S. Tunable directivity in metamaterials with reconfigurable cell symmetry. Applied Physics Letters 2015;106(9). doi:10.1063/1.4914011.

[21] Chen Y, Hu J, Huang G. A design of active elastic metamaterials for control of flexural waves using the transformation method. Journal of Intelligent Material Systems and Structures 2016;27(10):1337–47. doi:10.1177/1045389X15590273.

[22] Chen Y, Huang G, Sun C. Band gap control in an active elastic metamaterial with negative capacitance piezoelectric shunting. Journal of Vibration and Acoustics 2014;136(6):061008.

[23] Nouh M, Aldraihem O, Baz A. Periodic metamaterial plates with smart tunable local resonators. Journal of Intelligent Material Systems and Structures 2016;27(13):1829–45.

[24] Bloch F. Über die quantenmechanik der elektronen in kristallgittern. Zeitschrift für physik 1929;52(7-8):555–600.

[25] Hussein MI, Leamy MJ, Ruzzene M. Dynamics of Phononic Materials and Structures: Historical Origins, Recent Progress, and Future Outlook. Applied Mechanics Reviews 2014;66(4):040802. doi:10.1115/1.4026911.

[26] Mead D. Free wave propagation in periodically supported, infinite beams. Journal of Sound and Vibration 1970;11(2):181–97. doi:10.1016/S0022-460X(70)80062-1.

[27] Mead DJ. Vibration Response and Wave Propagation in Periodic Structures. Journal of Engineering for Industry 1971;93(3):783. doi:10.1115/1.3428014.

[28] Faulkner MG, Hong DP. Free vibrations of a mono-coupled periodic system. Journal of Sound and Vibration 1985;99(1):29–42. doi:10.1016/0022-460X(85)90443-2.

[29] Huang HH, Sun CT, Huang GL. On the negative effective mass density in acoustic metamaterials. International Journal of Engineering Science 2009;47(4):610–7.

[30] Pai PF. Metamaterial-based Broadband Elastic Wave Absorber. Journal of Intelligent Material Systems and Structures 2010;21(5):517–28. doi:10.1177/1045389X09359436.

[31] Hussein MI, Frazier MJ. Metadamping: An emergent phenomenon in dissipative metamaterials. Journal of Sound and Vibration 2013;332(20):4767–74.

[32] Frazier MJ, Hussein MI. Generalized bloch's theorem for viscous metamaterials: Dispersion and effective properties based on frequencies and wavenumbers that are simultaneously complex. Comptes Rendus Physique 2016;17(5):565–77.

[33] Chen Y, Barnhart M, Chen J, Hu G, Sun C, Huang G. Dissipative elastic metamaterials for broadband wave mitigation at subwavelength scale. Composite Structures 2016;136:358–71.

[34] Andreassen E, Jensen JS. Analysis of phononic bandgap structures with dissipation. Journal of Vibration and Acoustics 2013;135(4):041015.

[35] Hensley D. Continued fractions; vol. 20. World Scientific; 2006.

[36] Mathworks Documentation for MATLAB R2016b. `https://www.mathworks.com/help/control/ref/pole.html`; ???? Accessed: 2016-12-18.

[37] Singh T, Vadali SR. Robust time delay control. ASME Journal of Dynamic Systems, Measurement and Control 1993;115(2(A)):303–6.

[38] Singh T. Optimal reference shaping for dynamical systems: theory and applications. CRC Press; 2009.

[39] Martin G. On the control of flexible mechanical systems. Ph.D. thesis; Stanford University; 1978.

[40] Wie B, Bryson J. Modeling and control of flexible space structures. In: Dynamics and control of large flexiable aircrafts. 1981, p. 153–74.